Advanced Powder Technology 33 (2022) 103775

Contents lists available at ScienceDirect

Advanced Powder Technology

journal homepage: www.elsevier.com/locate/apt

Synthesis of novel halloysite@YF_3:Ce^{3+},Tb^{3+} nanocomposite for enhanced luminescent properties

Hongxia Peng [a], Liyi Liu [a], Jiaxi He [a], Jiahao Pi [a], Jianzhen Wu [c], Xiangni Wang [a], Xingping Huang [a], Xiaohe Liu [c,*], Fabiao Yu [b,*]

[a] Hunan Provincial Key Laboratory of Fine Ceramics and Powder Materials, Hunan University of Humanities, Science and Technology, Lou'di, Hunan 417000, PR China
[b] Laboratory of Neurology, the First Affiliated Hospital of Hainan Medical University, Key Laboratory of Hainan Functional Materials and Molecular Imaging, Key Laboratory of Emerg-ency and Trauma, Ministry of Education, Hainan Medical University, Haikou 571199, China
[c] State Key Laboratory of Powder Metallurgy and School of Materials Science and Engineering, Central South University, Changsha, Hunan 417000, PR China

ARTICLE INFO

Article history:
Received 19 January 2022
Received in revised form 8 August 2022
Accepted 24 August 2022

Keywords:
Halloysite
YF_3:Ce^{3+},Tb^{3+}
Luminescent property
Surface-interface-dielectric multiple confinement effect

ABSTRACT

A novel halloysite@YF_3: Ce^{3+}, Tb^{3+} anocomposite with strong luminescent properties was designed and synthesized by a facile direct precipitation strategy. Owing to the halloysite as a support, it can significantly prevent the aggregation of YF_3:Ce^{3+},Tb^{3+} and the distribution of YF_3:Ce^{3+},Tb^{3+} on halloysite was highly uniform. Importantly, due to the unique surface-interface-dielectric multiple confinement (SIDMC) effects, the as-harvested halloysite@YF_3:Ce^{3+},Tb^{3+} nanocomposite exhibited excellent luminescent performance. Compared with YF_3:Ce^{3+},Tb^{3+}, the luminescence intensity of halloysite@YF_3:Ce^{3+}, Tb^{3+} nanocomposite is significantly enhanced by about 6 times under 255 nm excitation. However, the fluorescence lifetime of halloysite@YF_3:Ce^{3+},Tb^{3+} nanocomposite (7.21 ms) is shorter than that of YF_3:Ce^{3+},Tb^{3+} nanoparticles (8.34 ms). This finding indicated that halloysite can change the luminescent properties of YF_3:Ce^{3+},Tb^{3+} nanoparticles through an SIDMC effect. The combination of halloysite and YF_3:Ce^{3+}, Tb^{3+} nanoparticles not only endowed halloysite with special properties, and effectively tuned the luminescent properties of YF_3:Ce^{3+},Tb^{3+} nanoparticles, thereby improving the utility of halloysite and YF_3:Ce^{3+},Tb^{3+} nanoparticles. The research supplies an insight on the development of natural mineral-based luminescent materials, and hopefully it could promote them application in many fields.

1. Introduction

Rare-earth luminescent materials have very important application value in the fields of display and image materials [1]. Rare-earth fluoride (YF_3:Ce^{3+},Tb^{3+}) is a good green fluorescent material because of its low phonon energy, high thermal stability, and good bio-compatibility [2]. However, it also has defects, such as easy agglomeration, low luminescent intensity, and limited resources [3]. More importantly, it accounts for approximately 30 % of the display cost as rare earth phosphor [4]. Therefore, preventing agglomeration, eliminating surface effects, improving luminescent intensity and utilization rate, and reducing display manufacturing costs of YF_3:Ce^{3+}, Tb^{3+} have become major subjects.

At present, methods for improving the emission intensity of rare-earth luminescent materials mainly include modulating matrix material (doped elements, such as Li^+, Zn^{2+}, Bi^{3+} and Ce^{3+}) [5–7]. However, controlling the concentration of the doping element and target substitution position is difficult, which easily leads to fluorescence quenching and an increase in the production cost. Another methods for improving the emission intensity of rare-earth fluoride is reducing fluorescence quenching by coating the inert shell (SiO_2) [8]. However, this method increases the size of the shell. More importantly, the inert shell (SiO_2) lacks chemical activity so it cannot further increase the luminescent intensity of rare-earth luminescent materials. In addition, the emission intensity of rare-earth fluoride can be enhanced by exposing different crystal faces and changing the electronic transition [9], and by coupling with localized surface plasmon resonance (LSPR) materials, such as noble metals (Ag/Au), oxygen-deficient metal oxides (W/MoO_{3-x}), and sulfides ($Cu_{2-x}S$) [10–12]. However, precious metals (Au or Ag) are expensive, and the morphology and defect

Peer review under responsibility of The copyright line should read:002: Copyright © 2014, The Society of Powder Technology Japan. Published by Elsevier BV and The Society of Powder Technology Japan. All rights reserved.001: Copyright © 2014 Published by Elsevier B.V. on behalf of The Society of Powder Technology Japan. All rights reserved.Please add this footnote for the item group IG000042 "This is the article featuring on ICBMH2019: the 13th International Conference on Bulk Materials Storage, Handling and Transportation."

* Corresponding authors.
E-mail address: 3197@huhst.edu.cn (X. Liu).

https://doi.org/10.1016/j.apt.2022.103775
0921-8831/

concentration of oxygen-deficient metal oxides and sulfides are difficult to control, so it is difficult to achieve wide application [13].

Recently, some studies reported that the fluorescence quantum yield of $NaGdF_4:Eu^{3+}$ nanoparticles can be improved by introducing Al_2O_3/SiO_2 with dielectric confinement effect [14–15]. The dielectric confinement effect is a phenomenon of enhanced dielectric properties due to the enhancement of the surfaces and inside local fields of the nanoparticles. However, the preparation process of Al_2O_3 and SiO_2 nanoparticles is complex, and their morphology and sizes are difficult to control. Thus, these nanoparticles have limited applications. Halloysite nanotube with specific surface is a good carrier of nanoparticles. Halloysite has many excellent properties, such as abundant reserves, low cost, high biocompatibility and environmentally friendliness [16], and thus it is widely used in bio-medicine, sewage treatment and other fields [17]. Halloysite is formed by dislocation and crimping of the silicon-oxygen tetrahedron and aluminum-oxygen octahedral lattices. Their aspect ratios are large, and their surface hydroxyl densities are low. Therefore, as support, they effectively offset the agglomeration of rare-earth fluorides nanoparticles [18]. Halloysite not only adjusts the structures, sizes, morphology, and dispersion of nanoparticles through its specific surface [19], but also changes their electronic structures and band gaps through the SIDMC effect [20].

The SIDMC effect is the general name for surface confinement, interface confinement, and dielectric confinement effects. The surface confinement effect is the effect of surface structure on the sizes, morphology, and properties of nanoparticles [21]. The interface effect refers to the response and characteristic of a nanocomposite material when it is subjected to physical and chemical actions [22]. The dielectric confinement effect is the enhancement of dielectric properties due to the enhancement of the surfaces and inside local fields of the nanoparticles [23].

We deposited monodispersed YF_3: Ce^{3+}, Tb^{3+} on halloysite to synthesize novel types of halloysite@YF_3:Ce^{3+},Tb^{3+} nanocomposites (Fig. 1). A combination of halloysite and YF_3:Ce^{3+}, Tb^{3+} can not only effectively tunes the luminescent intensity of YF_3:Ce^{3+}, Tb^{3+} nanoparticles through the SIDMC effect, but also endows halloysite with new functions. This research provides novel ideas and new methods for improving the utilization rate of halloysite while tuning the luminescent intensities and utilization rates of YF_3: Ce^{3+}, Tb^{3+} nanoparticles.

2. Experimental sections

2.1. Reagents

All reagents were of analytical grade and used without further purification. Halloysite was purchased from Xin Cheng Shen Fei Aluminum Alloy Co., ltd. (Wenzhou, China). Ammonium fluoride (NH_4F) was purchased from Beijing Chemical Works. $Y(NO_3)_3$, $Ce(NO_3)_3$ and $Tb(NO_3)_3$ were purchased from Science and Technology Parent Company of Changchun Institute of Applied Chemistry.

2.2. Preparation of halloysite@YF_3:Ce^{3+},Tb^{3+} nanocomposite

YF_3:Ce^{3+},Tb^{3+} nanoparticles were deposited on the surface of halloysite with a direct precipitation method. In a typical procedure, 0.5 g of halloysite was dispersed in 50 mL of H_2O and then 3.2 mL of $Y(NO_3)_3$, 1.2 mL of $Ce(NO_3)_3$ and 0.4 mL of $Tb(NO_3)_3$ solutions were added. The mixture was sonicated for 10 min before the addition of 10 mL of NH_4F (0.6 mol/L) solution, and then heated to 75 °C under vigorous mechanical stirring. After 2 h, the resultant products were washed with ethanol and deionized water and dried for 4 h at 60 °C.

2.3. Characterization

X-ray diffraction (XRD) patterns of the samples were measured using an AXS D8 Advance diffractometer (Bruker, Bremen,Germany) with Cu Ka radiation (λ = 0.15406 nm) at 40 kV and 40 mA. Scanning electronic microscopy (SEM) images were recorded on a Hitachi S-4800 microscope. Transmission electron microscopy (TEM), EDS, HRTEM and SAED (FEI, Tecnai T20, Netherland) were carried out after dissolving all samples in ethanol and mounted them in a copper grid. The UV/Vis light absorption performance was analyzed by UV 3600 spectrometer. A Bruker Vertex 70 infrared spectrometer was used for FTIR analysis. The valence states of the elements were analyzed by X-ray photoelectron spectroscopy (XPS) Thermo Scientific K-Al pha +. The X-ray source was Al Ka micro-focusing monochromatic source which the beam spot was continuously adjustable from 30 to 400 um, and the step size was 5 um. The photoluminescence (PL) spectra, PL quantum yield and PL lifetimes were recorded on an Edinburgh FLS1000 fluorescence spectrometers. The quantum yield was measured by using $BaSO_4$ standard sample as reference. The fluorescence lifetime was measured with 375 nm-EPL as excitation light source and 542 nm as fluorescence monitoring wavelength, and then the fluorescence decay data were collected and fitted at room temperature. Agilent 4294A impedance analyzer was used for dielectric constant and dielectric loss analysis at room temperature.

3. Result and discussion

3.1. XRD, SEM and TEM analysis

The structure and composition of the halloysite@YF_3:Ce^{3+},Tb^{3+} nanocomposite were determined through XRD measurements (Fig. 2). In the XRD pattern of the nanocomposite, besides the characteristic reflections (2θ = 21.08°, 26.23°, 34.92°, 62.76°) of the monoclinic phase of halloysite (JCPDS.29–1487), and the diffraction (2θ = 26.23°, 28.38°, 44.90°, 46.22°, 52.23°) of the orthogonal phase of YF_3:Ce^{3+},Tb^{3+} (JCPDS. 05–0392), no diffraction peaks of impurities were detected, revealing the final product as the halloysite@YF_3:Ce^{3+},Tb^{3+} nanocomposite.

The morphological characteristics of the halloysite@YF_3:Ce^{3+}, Tb^{3+} nanocomposite were observed through SEM analysis. As shown in Fig. 3a, c, halloysite had an obvious rod-like structure and smooth surface. After YF_3: Ce^{3+}, Tb^{3+} nanoparticles were deposited on the surface of halloysite, they retained rod shapes and showed slight aggregation (Fig. 3b and d). Compared with halloysite, the roughness and looseness of the surface of the halloysite@YF_3:Ce^{3+},Tb^{3+} nanocomposite increased (Fig. 3d). More importantly, isolated YF_3: Ce^{3+},Tb^{3+} nanoparticles were not observed in Fig. 3d, which indicates that YF_3:Ce^{3+},Tb^{3+} nanoparticles were fully deposited on the surface of halloysite.

The morphology of the as-prepared halloysite@YF_3:Ce^{3+},Tb^{3+} nanocomposite was characterized using transmission electron microscopy (TEM) and high-resolution TEM (HRTEM), as shown in Fig. 4. The halloysite@YF_3:Ce^{3+},Tb^{3+} nanocomposite exhibited a typical tubular nanostructure with an inter diameter and outer diameter of approximately 30 and 40 nm (Fig. 4A). The HRTEM image of the halloysite@YF_3:Ce^{3+},Tb^{3+} nanocomposite (Fig. 4B) clearly demonstrated that the nanoparticles bound tightly to the surface of halloysite. Their lattice spacing values were approximately 0.313 and 0.343 nm, which corresponded to the (1 1 1) and (0 2 0) planes of YF_3:Ce^{3+},Tb^{3+}, confirming that the nanoparticles were YF_3:Ce^{3+},Tb^{3+} crystals. Halloysite plays an important role in the growth of YF_3:Ce^{3+},Tb^{3+} nanoparticles on a halloysite surface. In the halloysite@YF_3:Ce^{3+},Tb^{3+} nanocomposite, many nanoparticles with mean sizes of 20.03 nm ($n = 100$) were uniformly coated

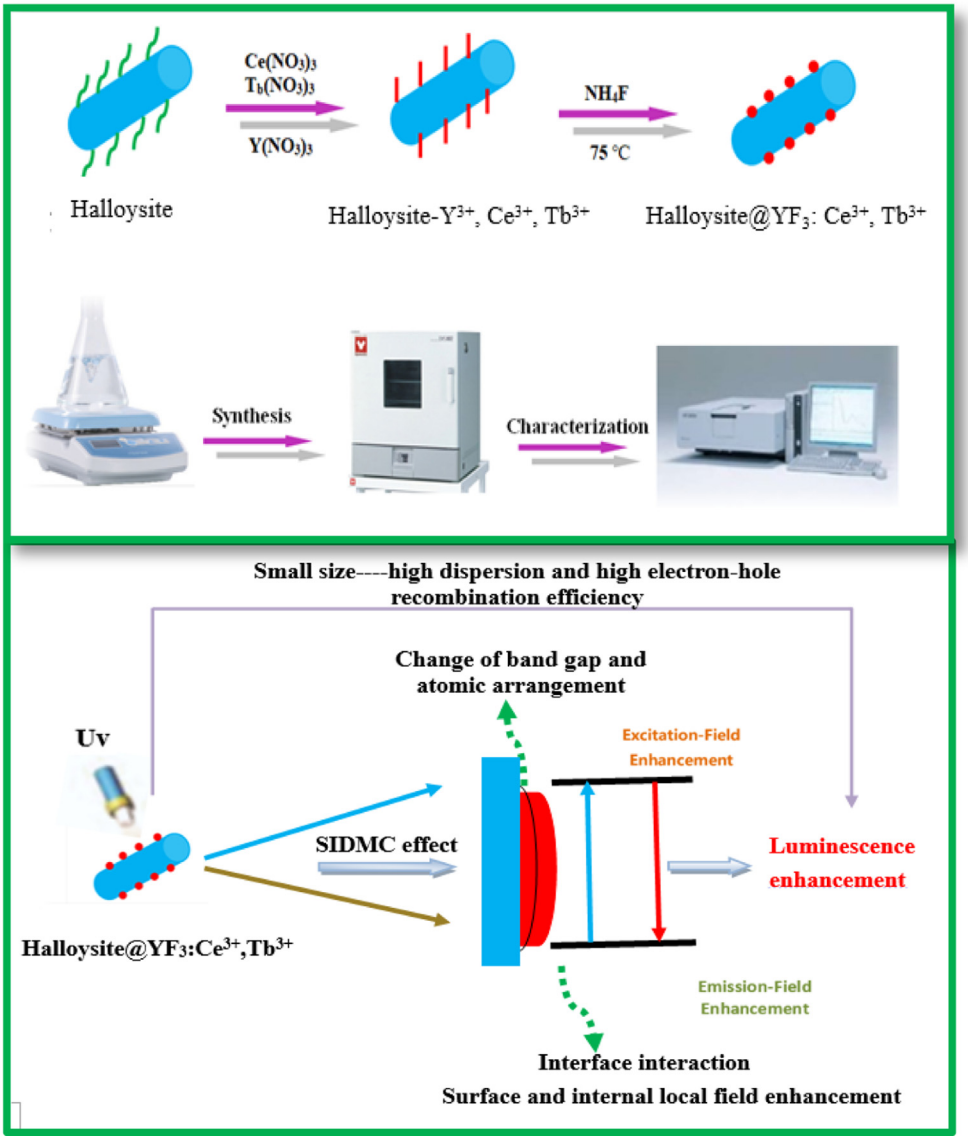

Fig. 1. Synthesis procedure and schematic illustration of luminescence enhancement mechanism of halloysite@YF_3:Ce^{3+},Tb^{3+} nanocomposite.

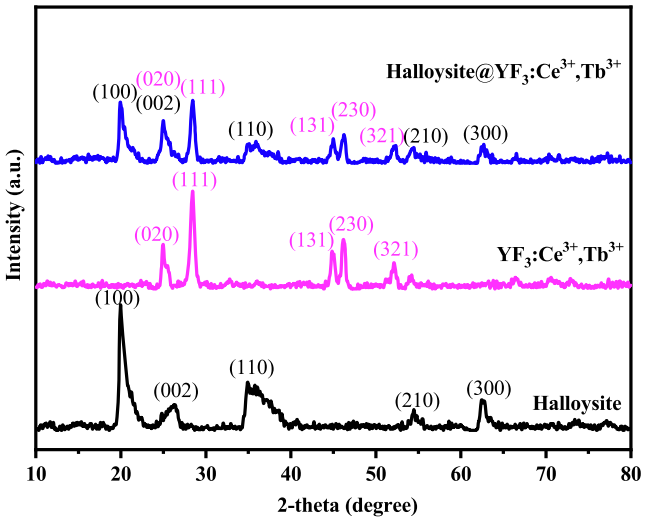

Fig. 2. XRD patterns of halloysite, YF_3:Ce^{3+},Tb^{3+} and halloysite@YF_3:Ce^{3+},Tb^{3+} nanocomposite.

on the halloysite surface (Fig. 4A). Y^{3+} ions were adsorbed on the negatively-charged halloysite surface, and then nucleation and growth of YF_3:Ce^{3+},Tb^{3+} occurred on the halloysite surface (Fig. 1).

Owing to the surface confinement of halloysite, the growth and aggregation of YF_3:Ce^{3+},Tb^{3+} were inhibited, thus leading to the formation of uniform YF_3:Ce^{3+},Tb^{3+} nanoparticles. In addition, no single halloysite nor YF_3:Ce^{3+},Tb^{3+} nanoparticles was observed. Fig. 4C shows the SAED patterns obtained from the halloysite@YF_3:Ce^{3+}, Tb^{3+} nanocomposite, and polycrystalline diffraction rings consisted of discrete diffraction spots. The halloysite@YF_3:Ce^{3+},Tb^{3+} nanocomposite were successfully fabricated with the method used in this work.

The composition of the halloysite@YF_3:Ce^{3+},Tb^{3+} nanocomposite was determined through EDX analysis, as shown in Fig. 5 a-h. Fig. 5b-h is the distribution map of Al, Si, O, Y, F, Ce, and Tb. All the elements were evenly distributed. TEM and EDX analysis further confirmed the formation of the nanocomposites. The combination of halloysite and YF_3:Ce^{3+},Tb^{3+} nanoparticles can enhance the luminescent intensity of YF_3:Ce^{3+},Tb^{3+} nanoparticles. Halloysite performed a new function (luminescence), and the utilization rate of halloysite was improved.

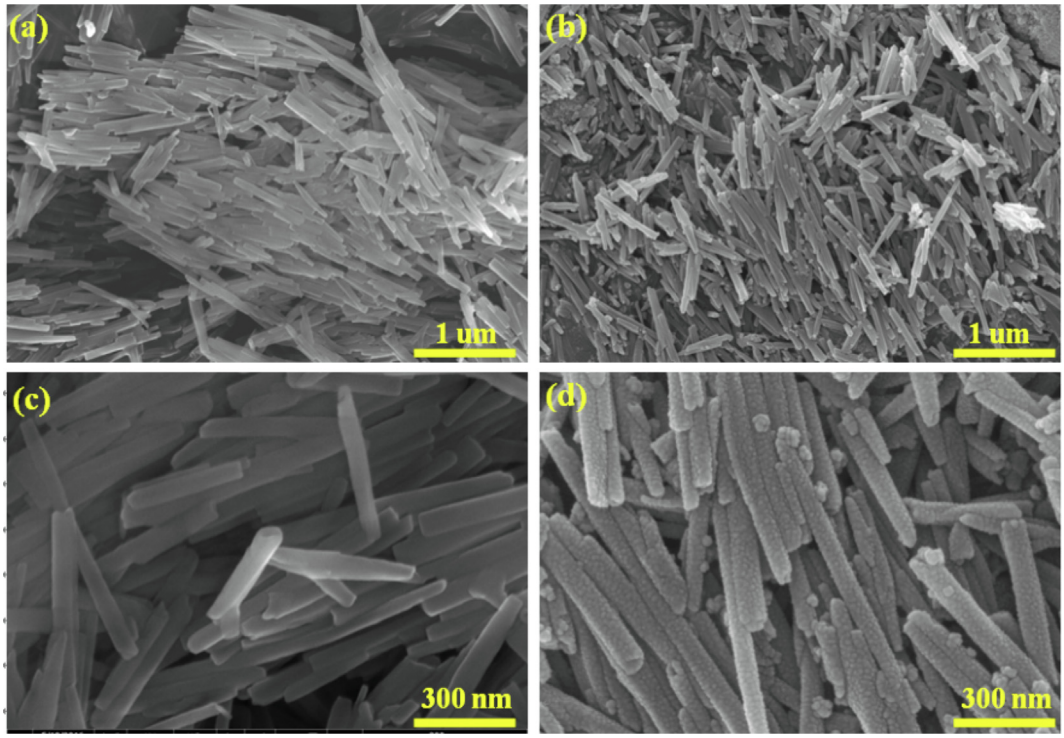

Fig. 3. SEM of halloysite (a, c) and halloysite@YF_3:Ce^{3+},Tb^{3+} (b, d) nanocomposite.

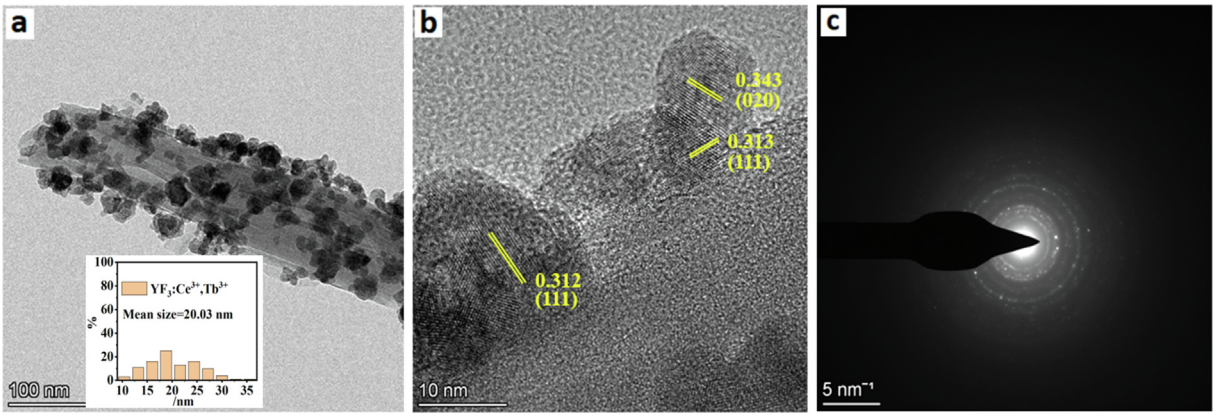

Fig. 4. (a) TEM image and (inset) corresponding particle size distribution histogram, (b) HRTEM image, and (c) SAED pattern of halloysite@YF_3:Ce^{3+},Tb^{3+} nanocomposite.

3.2. FT-IR analysis

Fig. 6 shows the infrared spectra of halloysite, YF_3:Ce^{3+},Tb^{3+} and halloysite@YF_3: Ce^{3+},Tb^{3+}. Halloysite generated strong splitting peaks at 3697 and 3619 cm^{-1} in the high-frequency region, which were attributed to the stretching vibration absorption peaks of the inner tube wall OH of halloysite. The deformation vibration absorption peak of H_2O molecule appeared at 1637 cm^{-1} in the middle frequency region. In the low frequency region, the absorption peaks at 1040 cm^{-1} were attributed to the telescopic vibration band of the -Si-O- bond. The absorption peak at 910 cm^{-1} and 759 cm^{-1} came from the OH flexural vibration band and the Si-O flexural vibration absorption. The absorption peaks at 689 and 543 cm^{-1} were attributed to the vibration bands of Al-O-Si and Si-O-Si, respectively[24]. In the spectrum of YF_3:Ce^{3+},Tb^{3+}, the H—O—H stretching vibration peak appeared in the high-frequency region of 3300–3500 cm^{-1}. In the intermediate frequency region, the bending vibration absorption peaks of H—O—H and the vibration absorption peaks of NO_3^- appeared at 1637 and 1424 cm^{-1}, respectively[25]. In the low frequency region, the absorption peaks at 1070 cm^{-1} came from the absorption peaks of C—O (CO_2 absorbed on the surface of YF_3:Ce^{3+},Tb^{3+}) [25].

When YF_3: Ce^{3+}, Tb^{3+} were coated on the surface of halloysite, three absorption peaks appear at 3697, 3619 and 3440 cm^{-1} in the spectrum of halloysite@YF_3: Ce^{3+},Tb^{3+}, because of the stretching and bending vibration absorption of –OH [25]. In the low frequency region, the absorption peaks at 1070 and 1040 cm^{-1} came from the absorption peaks of C—O (CO_2 absorbed on the surface of YF_3:Ce^{3+},Tb^{3+}) and the stretching vibration absorption peak of the Si-O- bond [26]. Compared with the spectra of halloysite, the flexural vibration absorption peak of Si-O at 759 cm^{-1} and the flexural vibration peaks of Al-O-Si and Si-O-Si at 685 cm^{-1} and 543 cm^{-1} gradually weakened, indicating that YF_3:Ce^{3+},Tb^{3+} was successfully coated on the surface of halloysite [26]. The H—O—H stretching vibration peak (at 3340 cm^{-1}) and the H—O—H bending vibration absorption peak (at 1637 cm^{-1}) in the spectra of

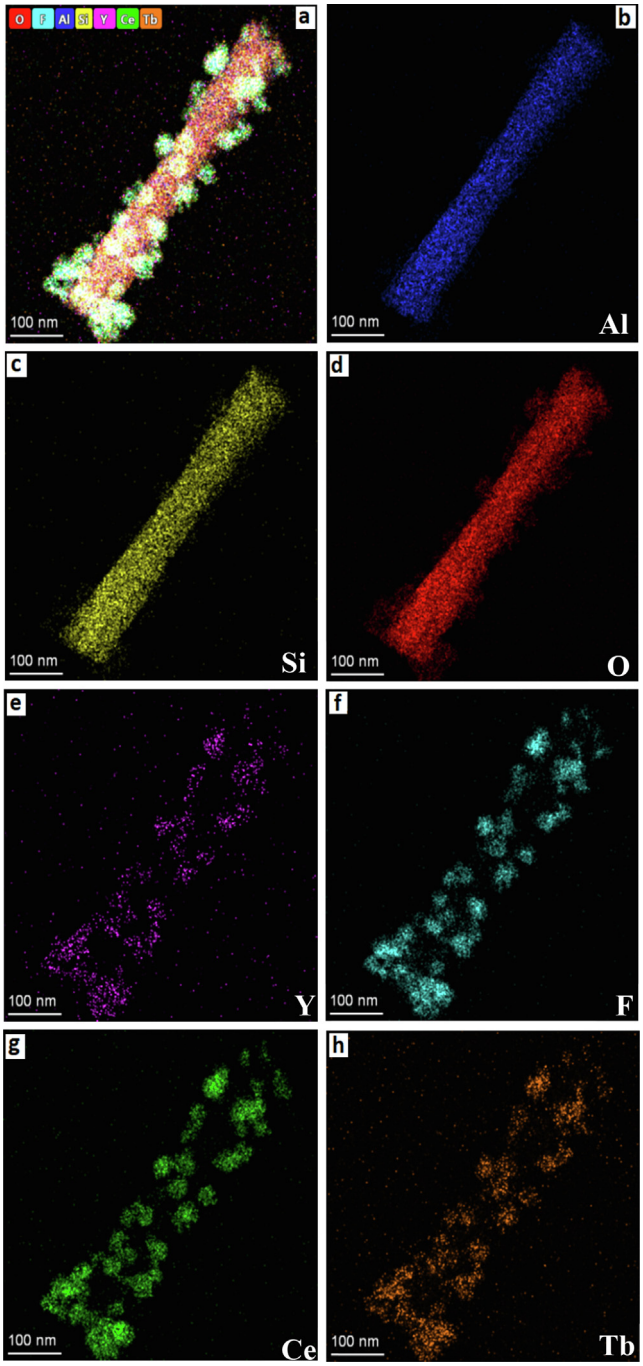

Fig. 5. (a) TEM images of halloysite@YF_3:Ce^{3+},Tb^{3+} nanocomposite; (b–h) energy dispersive X-ray (EDX) mapping of halloysite@YF_3:Ce^{3+},Tb^{3+} nanocomposite.

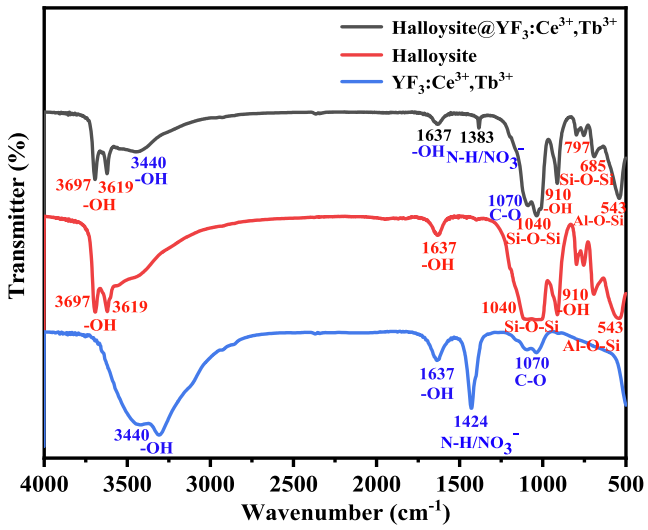

Fig. 6. Infrared spectrum of halloysite, YF_3:Ce^{3+}, Tb^{3+} and halloysite@YF_3:Ce^{3+},Tb^{3+} nanocomposite.

halloysite@YF_3:Ce^{3+},Tb^{3+} nanocomposite were weaker that those in the spectra of YF_3:Ce^{3+}, Tb^{3+}. This result confirmed that YF_3: Ce^{3+}, Tb^{3+} was deposited on the surface of halloysite. When YF_3:Ce^{3+}, Tb^{3+} was deposited on the surface of halloysite, which reduced or removed the partial groups on the surface of YF_3:Ce^{3+}, Tb^{3+}, the emission intensity of YF_3:Ce^{3+}, Tb^{3+} improved.

3.3. XPS analysis

Furthermore, the interactions at the halloysite-YF_3:Ce^{3+},Tb^{3+} interfaces were investigated by XPS analysis. Fig. 7a shows the XPS full spectrum of halloysite@YF_3:Ce^{3+},Tb^{3+} nanocomposite. It can be seen from the full spectrum that the halloysite@YF_3:Ce^{3+}, Tb^{3+} nanocomposite consists of Al, Si, O, Y, F, Ce, and Tb elements. Because of the penetration depth of XPS is about 5–8 nm, which indicates that the thickness of YF_3:Ce^{3+},Tb^{3+} layers in halloysite@YF_3:Ce^{3+},Tb^{3+} nanocomposite is only a few nanometers. The incident area of XPS is near the interface between halloysite and YF_3:Ce^{3+},Tb^{3+} shells, which shows that the detected results reflect the characteristics of halloysite@YF_3:Ce^{3+},Tb^{3+} heterojunction interface.

Besides that, the high-resolution O 1 s, Si 2p, Al 2p, Y 3d, Ce 3d, Tb 3d, and F 1 s XPS spectra were also collected to analyze the bonding environments of the coated YF_3:Ce^{3+},Tb^{3+}. The O 1 s peak shifted from 531.78 to 534.39 eV after the YF_3:Ce^{3+},Tb^{3+} combined with halloysite (Fig. 7b), indicating that the oxygen-bearing groups of the halloysite interacted strongly with YF_3:Ce^{3+},Tb^{3+}. In addition, the Si 2p and Al 2p binding energies also increased from 102.85 and 74.52 to 105.27 and 77.64 eV after coating YF_3:Ce^{3+},Tb^{3+}, respectively (Fig. 7c and d), indicating the bonding of YF_3:Ce^{3+}, Tb^{3+} on halloysite component.

The details of the combination of YF_3:Ce^{3+},Tb^{3+} and halloysite also can be found in the changes in the Y 3d, Ce 3d, Tb 3d, and F 1 s spectra. Before the combination, the Y 3d spectrum displayed doublets centered at 159.08 eV for Y $3d_{5/2}$ and 161.07 eV for Y $3d_{3/2}$. After the combination, the binding energies of the Y $3d_{3/2}$ increased by $\sim$ 0.5 eV, further revealing the bonding interaction of Y^{3+} with HNT–OH. Before the combination, the Ce 3d spectrum displayed doublets centered at 885.55 eV for Ce $3d_{5/2}$ and 904.30 eV for Ce $3d_{3/2}$. After the combination, the binding energy of Ce $3d_{5/2}$ and Ce $3d_{3/2}$ increased by approximately 2.1 eV, and this was attributed to the HNT–O–Ce^{3+} complexation between the structural HNT–O and combined Ce^{3+}. Before the combination, the Tb 3d spectrum displayed doublets centered at 1242.66 eV for Tb $3d_{5/2}$ and 1277.19 eV for Tb $3d_{3/2}$. After the combination, the binding energy of Ce $3d_{5/2}$ and Ce $3d_{3/2}$ increased by approximately 3.82 and 2.59 eV respectively, and this was attributed to the HNT–O–Tb^{3+} complexation between the structural HNT–O and combined Tb^{3+}.

In addition, the F 1 s binding energies also increased from 684.85 to 687.81 eV after the combination (Fig. 7c and d), indicating the bonding of YF_3:Ce^{3+},Tb^{3+} on halloysite component. Moreover, we conducted composition analysis of the halloysite@YF_3:Ce^{3+},Tb^{3+} nanocomposite via TEM elemental mapping with Al, Si,

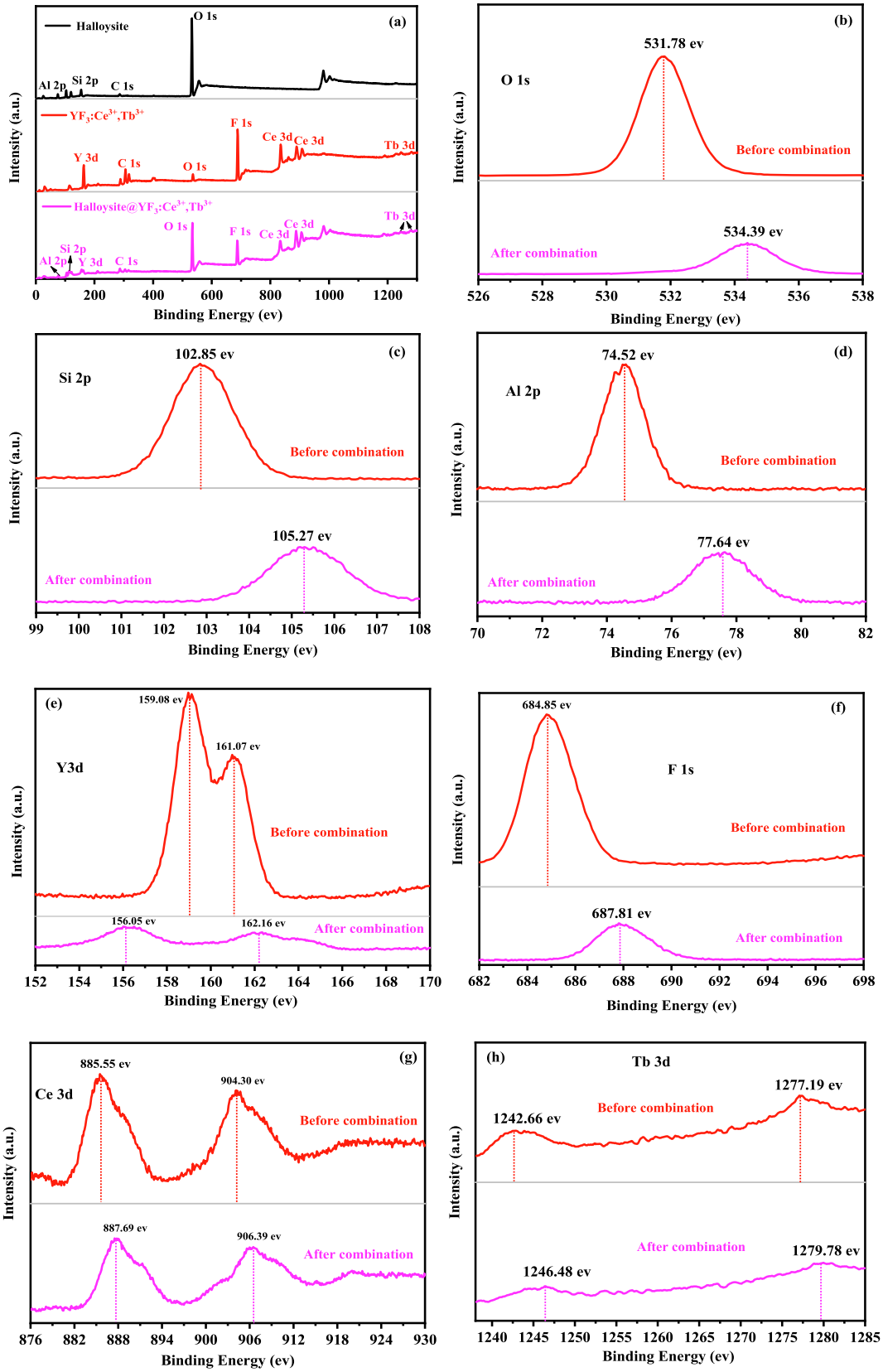

Fig. 7. XPS spectra (a) XPS survey spectra of halloysite, $YF_3:Ce^{3+},Tb^{3+}$ and halloysite@$YF_3:Ce^{3+},Tb^{3+}$ nanocomposite and High-resolution O 1 s(b), Al 2p(c), Si 2p(d), Y 3d (e), F 1 s(f), Ce 3d(g), Tb 3d(h).

O, Y, F, Ce, and Tb, further demonstrating that the YF_3:Ce^{3+},Tb^{3+} shell is located on the surface of the halloysite.

3.4. UV–vis and UV–vis DRS spectra analysis

Fig. 8A-C shows the UV–vis and UV–vis DRS spectra of YF_3:Ce^{3+}, Tb^{3+} and halloysite@YF_3:Ce^{3+},Tb^{3+} nanocomposite, respectively. As shown in Fig. 8A, the halloysite@YF_3:Ce^{3+},Tb^{3+} nanocomposite showed an obvious optical absorption in the UV–vis region (200–600 nm), indicating that the halloysite@YF_3:Ce^{3+},Tb^{3+} nanocomposite possessed unique optical properties. Compared to that of individually dispersed halloysite (4.338 ev, Fig. 8B), the absorption edge of halloysite@YF_3:Ce^{3+},Tb^{3+} nanocomposite has an obvious red shift of about 100 nm, which can be attributed to the heteroepitaxial growth of YF_3:Ce^{3+},Tb^{3+} on the halloysite surface. As shown in Fig. 8D, the band gaps of the halloysite@YF_3:Ce^{3+}, Tb^{3+} nanocomposites are about 2.12 eV. Better than YF_3:Ce^{3+},Tb^{3+} (Fig. 8B, 4.34 eV) nanoparticles and halloysite, halloysite@YF_3: Ce^{3+},Tb^{3+} nanocomposites with a narrow band gap should have a high light adsorb activity in the UV–vis region and was suitable for light emission under different excitation wavelengths. But band gap modification is significative, which explain that halloysite have effect to band gap of YF_3:Ce^{3+},Tb^{3+}. The significative change in the band gap values can be attributed to the combined effects of surface-interfacial defects. The results of XRD analysis showed the low crystallinity of YF_3:Ce^{3+},Tb^{3+} layer in the nanocomposite.

The low crystallinity increased crystal defects. The growth of these defects at a specific concentration would generate the defect energy level, and defects dispersed and overlapped with the edge of the conducting band [27]. These effects led to the narrowing of the band gap of the YF_3:Ce^{3+},Tb^{3+} nanoparticles on the surface of halloysite. This result was consistent with the analysis of UV-absorption spectrum [27]. The obvious influence of halloysite on the band gap of YF_3:Ce^{3+},Tb^{3+} nanoparticles may be related to the content of interface defects.

In the halloysite@YF_3:Ce^{3+},Tb^{3+} nanocomposite, the increase in interface defect concentration produced the overlap of the wave functions in defect states, which split the separated defect energy levels into energy bands. The width of the defect energy band is proportional to the defect concentration [28]. The wide defect band led to the overlapping of defect band with the conduction band, moving the conduction band downwards and thus narrowing down the band gap.

3.5. Urbach tail energy

To obtain evidence of increment in localized defect states and change in the structural disorderliness of the material, we calculated Urbach tail energy by using Eq. (1), where α is absorption coefficient, α_0 is a constant, h is the Planck constant, v is the frequency of photon and E_u is the Urbach tail energy. The value was calculated from the inverse of the slope by using the plot of $\ln(\alpha)$ and hv and the obtained results for YF_3: Ce^{3+}, Tb^{3+} nanoparticles and the halloysite@YF_3:Ce^{3+},Tb^{3+} nanocomposite were 0.251 and 0.505 ev, respectively (Fig. 9).

$$\alpha(\mathrm{v}) = \alpha_0 exp\frac{h\upsilon}{E_u}\alpha(\upsilon) = \alpha_0 exp\frac{h\upsilon}{E_u} \quad (1)$$

α can be obtained from formula (2).

$$\alpha = 2.303 \times \frac{A}{t} \quad (2)$$

Where A is the light absorption intensity and t is the thickness of the samples (t = 1 mm).

From the definition of Urbach tail energy, we can find that any material showing high or low Urbach energy has a large or small number of defect states. The results showed that the

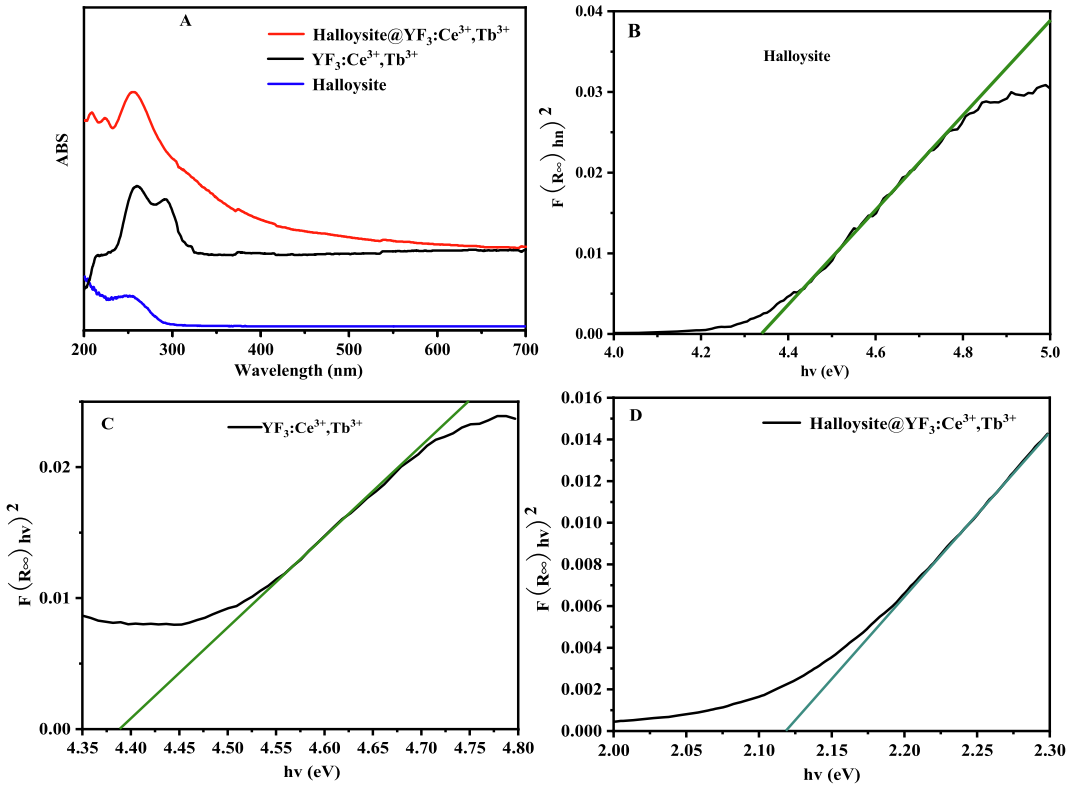

Fig. 8. (A) UV–*vis* spectra of samples; (B, C, D) DRS spectra of samples with the corresponding plots of $[F(R\infty)hv]^2$ versus hv.

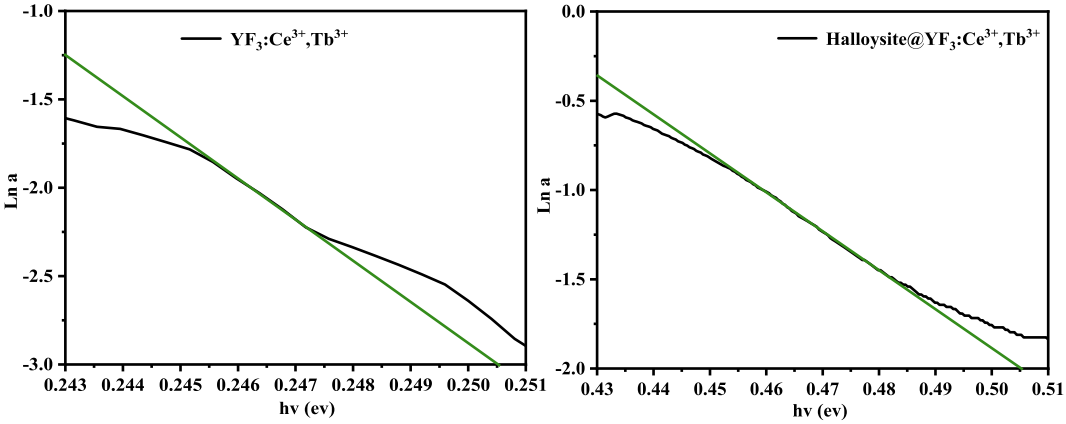

Fig. 9. Urbach tail energy fitting of YF_3:Ce^{3+},Tb^{3+} and halloysite@YF_3:Ce^{3+},Tb^{3+} nanocomposite.

halloysite@YF_3:Ce^{3+},Tb^{3+} nanocomposite had a larger Urbach energy than YF_3:Ce^{3+},Tb^{3+} nanoparticles, implying the larger density of defect states, that is, surface, interface, interstitial, or any kinds of defects. Therefore, according to the Urbach energy values, halloysite can act as a good carrier for YF_3:Ce^{3+},Tb^{3+} nanoparticles, and the emission intensity of YF_3:Ce^{3+},Tb^{3+} nanoparticles can be enhanced.

3.6. Dielectric properties

Dielectric constant and dielectric loss are two important indicators for evaluating the dielectric properties of materials. In a luminescent nanocomposite, the dielectric confinement effect plays a vital role in the regulation of its luminescence performance [20]. According to the literature [29], the dielectric constant of halloysite is lower than 2.90, and the dielectric loss is lower than 0.005. As shown in Fig. 10A, B, the dielectric constant of YF_3: Ce^{3+}, Tb^{3+} nanoparticles was lower than 60.00, and the dielectric loss was lower than 4.00. Moreover, as frequency decreased, its dielectric constant and dielectric loss gradually weakened. As shown in Fig. 10A, B, the dielectric constant and dielectric loss of the halloysite@YF_3:Ce^{3+},Tb^{3+} nanocomposite improved to a certain extent. The main reason was that the interface polarization effect occurred at the interface of halloysite and YF_3: Ce^{3+}, Tb^{3+}, which increased the accumulation of electrons at the interface. As the frequency increased, the dielectric constant and dielectric loss factor gradually decreased. The above results showed that halloysite combined with YF_3:Ce^{3+}, Tb^{3+} nanoparticles, and a strong dielectric confinement effect was produced at their interface and enhanced the emission intensity of the halloysite@YF_3:Ce^{3+}, Tb^{3+} nanocomposite.

3.7. Luminescent properties

To investigate the luminescence properties of the nanoparticles, we recorded the photoluminescence (PL) spectra at room temperature, Fig. 10. In the excitation spectra (Fig. 10C) monitored with 542 nm emission of Tb^{3+}, the strong excitation band at 255 nm can be assigned to the absorption of *4f–4f5d* band of Ce^{3+}. In the emission spectra (Fig. 10D) obtained by the excitation at 255 nm, the weak emission peaks centered at 379 nm are assigned to the *5d–4f* transition of the Ce^{3+} ion [30,31], and the characteristic strong transition lines of Tb^{3+} ($^5D_4$-^7F_J, J = 6, 5, 4, 3) can be observed. It can be seen that the dominant emission is centered at 542 nm due to the $^5D_4$-$^7F_5$ transition. It figures out that energy has been effectively transferred from Ce^{3+} to Tb^{3+} in the YF_3:Ce^{3+},Tb^{3+} and halloysite@YF_3:Ce^{3+},Tb^{3+} nanocomposites. Additionally, as shown in Fig. 10D, the intensity of both excitation and emission spectra of halloysite@YF_3:Ce^{3+},Tb^{3+} increases comparing with YF_3:Ce^{3+}, Tb^{3+}. And the quantum yield of YF_3:Ce^{3+},Tb^{3+} and halloysite@YF_3:Ce^{3+},Tb^{3+} was also measured, which was 8.53 % and 91.70 %, respectively. This further proves that the luminescence intensity of YF_3:Ce^{3+},Tb^{3+} is enhanced by halloysite.

Fig. 11 show the decay curves of the prepared YF_3:Ce^{3+},Tb^{3+} and halloysite@ YF_3:Ce^{3+},Tb^{3+} nanocomposite. The fluorescence decay curves of YF_3:Ce^{3+},Tb^{3+} and halloysite@YF_3:Ce^{3+},Tb^{3+} nanocomposite conform to the dual-exponential decay behavior, and the dual-exponential function is adopted:

$$I(t) = \alpha_1 e^{(-t/\tau_1)} + \alpha_2 e^{(-t/\tau_2)} \quad (1)$$

Where I is the fluorescence intensity, τ_1 and τ_2 are the fast process and slow process of fluorescence decay, α_1 and α_2 are the fitting index of the two processes. Its average fluorescence lifetime (τ) is calculated by formula (2):

$$\tau = (\alpha_1\tau_1^2 + \alpha_2\tau_2^2)/(\alpha_1\tau_1 + \alpha_2\tau_2) \quad (2)$$

Based on the formula (2), the fluorescence lifetime of YF_3: Ce^{3+}, Tb^{3+} and halloysite@YF_3:Ce^{3+}, Tb^{3+} nanoparticles is 8.34 ms and 7.21 ms, separately. It can be seen from Fig. 9 that the fluorescence lifetime of the halloysite@YF_3:Ce^{3+}, Tb^{3+} nanoparticles is shorter than that of YF_3:Ce^{3+},Tb^{3+} nanoparticles. Combined with the above fluorescence spectral analysis, it can be seen that the quantum yield is accompanied by the weakening of the fluorescence lifetime.

$$T = (K_t + K_{nr})^{-1} \quad (3)$$

$$¢= Kt\ T \quad (4)$$

where T is the fluorescence lifetime, Kt is the radiation attenuation probability, Knr is the non-radiation attenuation probability, ¢ is the quantum yield.

The experimental results show that the fluorescence lifetime becomes shorter with the enhancement of fluorescence intensity. It can be approximated that the fluorescence lifetime becomes shorter with the increase of quantum yield. According to formula (4), the radiation transition attenuation Kt is significantly increased, and the non-radiation attenuation Knr represents consumption in the form of heat, which is neglected. The value derived from formula (3) is weakened and is consistent with the experimental results.

The above analysis results indicated the reason for the stronger emission intensity of halloysite@YF_3:Ce^{3+},Tb^{3+} nanocomposite as compared with YF_3:Ce^{3+}, Tb^{3+} nanoparticles (Fig. 1). First, the YF_3:Ce^{3+},Tb^{3+} nanoparticles coated on the surface of halloysite, which weakened or reduced the surface lattice distortion, dangling bonds, surface adsorption and surface defects, eliminated the negative effects of the surface on the luminescence properties of YF_3:

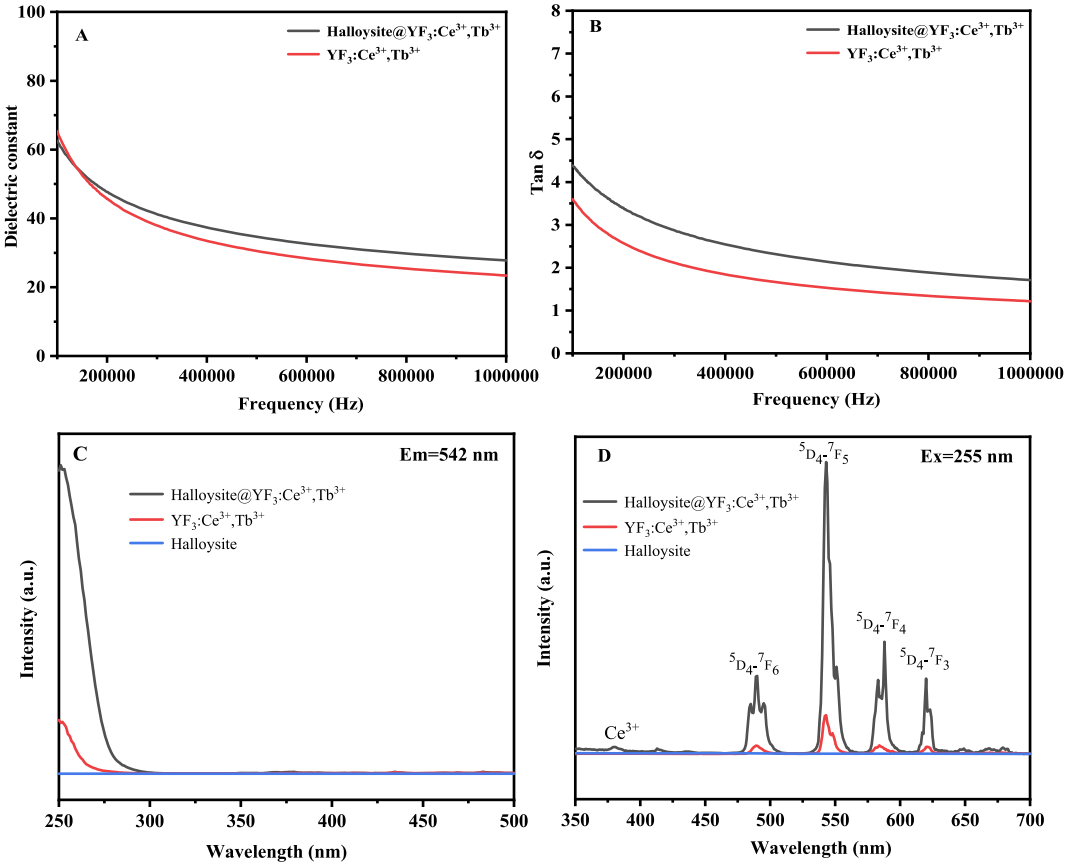

Fig. 10. Dielectric performance of $YF_3:Ce^{3+},Tb^{3+}$ and halloysite@$YF_3:Ce^{3+},Tb^{3+}$: (A) dielectric constant and (B) tan δ; (C) and (D) Excitation and emission spectra of halloysite@$YF_3:Ce^{3+}$, Tb^{3+}; $YF_3:Ce^{3+},Tb^{3+}$ and halloysite.

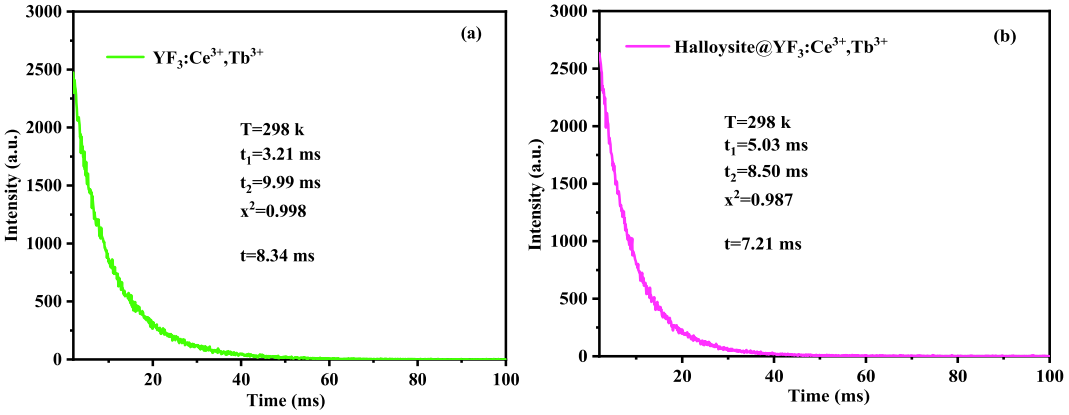

Fig. 11. Fluorescent decay curves of *5D4* → *7F5* (552 nm) for Tb^{3+}.

Ce^{3+},Tb^{3+} nanoparticles. Moreover, it eliminated the interference of the external environment to the rare earth ions (Ce^{3+}, Tb^{3+}), thereby enhancing the emission intensity of the $YF_3:Ce^{3+},Tb^{3+}$ nanoparticles. Second, the surface-interface and the effect of dielectric confinement field between halloysite and YF_3: Ce^{3+},Tb^{3+} nanoparticles reduced the particle size of $YF_3:Ce^{3+},Tb^{3+}$ nanoparticles, improved their dispersibility, and reduced the band gap and radiation recombination probability. Third, the dielectric confinement effect enhanced the surface and internal local field strength of the crystals, thereby enhancing the luminescence intensity of the $YF_3:Ce^{3+},Tb^{3+}$ nanoparticles. Owing to the micro-interference effect of the crystal field in the solid material system, only the rare earth ions doped in the matrix lattice were excited to produce radiation transitions. The rare earth ions exposed on the surface of the matrix material or close to the surface of the matrix material were difficult to be excite because the boundary of the gas–solid interface was hardly disturbed by the degraded crystal field on the surface of the matrix [31]. Under the synergy of the degraded crystal field and coordination field on the surface of the matrix, the rare earth ions near the surface of the matrix were excited by the combination of halloysite and $YF_3:Ce^{3+},Tb^{3+}$ nanoparticles. Compared with the method of enhancing the luminescent intensity of rare earth luminescent materials through the core–shell structure strategy, the method of introducing halloysite (SIDMC effects) in this

paper is more suitable for preparing novel rare earth luminescent materials that have low costs, can be easily prepared, can be prepared through batch production, and have excellent properties. Emission wavelength and intensity can be adjusted by changing the excitation wavelength.

4. Conclusions

A new type of halloysite@YF_3:Ce^{3+},Tb^{3+} nanocomposite was successfully synthesized with the direct precipitation method. The combination of halloysite and YF_3:Ce^{3+},Tb^{3+} nanoparticles not only endowed halloysite with new functions but also improved the luminescence properties of YF_3:Ce^{3+},Tb^{3+} nanoparticles through SIDMC effect because of the heteroepitaxial growth of YF_3:Ce^{3+},Tb^{3+} nanoparticles on the surface of halloysite. Moreover, the combination of halloysite and YF_3:Ce^{3+},Tb^{3+} nanoparticles increases the concentration of excitable $Ce^{3+}$and Tb^{3+} ions and reduce the surface defects of YF_3:Ce^{3+},Tb^{3+} nanoparticles. The prepared novel halloysite@YF_3:Ce^{3+},Tb^{3+} nanocomposite have broad application prospects in various fields, such as lighting lamps and displays, and can be used in visualizing orally administered drug delivery carriers. The synthesis strategy has the following merits: high output, a simple reaction device, and mild conditions. This strategy can be used in synthesizing other natural mineral-based luminescent nanocomposites and provides an experimental basis for the development of novel low-cost luminescent materials.

Declaration of Competing Interest

The authors declare that they have no known competing financial interests or personal relationships that could have appeared to influence the work reported in this paper.

Acknowledgements

This work was supported by hunan natural science foundation of China (grant number 2022JJ30315); the Scientific research project of Hunan province department of education (19A264); the planned science and technology project of Hunan province, China (grant number 2016TP1028); the double first-class discipline construction program of Hunan province.

Author Contribution

Liyi Liu and Hongxia Peng conceived and designed the experiments, and Hongxia Peng supervised the research; Jiahao Pi, Xingping Huang and Xiangni Wang helped to synthesize the halloysite@YF_3:Ce^{3+},Tb^{3+} nanocomposites; Jianzhen Wu helped to examine the halloysite@YF_3:Ce^{3+},Tb^{3+} nanocomposites; Liyi Liu and Jiaxi He performed the synthesis and characterization, interpreted the data and wrote the paper with help from Fabiao Yu and Xiaohe Liu.

References

[1] D. Hu, H. Peng, Y. Peng, J. Guo, Synthesis and enhanced luminescence properties of CuS@YF_3: Eu core–shell nanoparticles, Appl. Phy. A. 126 (5) (2020).
[2] J. Xie, W. Hu, D. Tian, Y. Wei, G. Zheng, L. Huang, E. Liang, Selective growth and upconversion photoluminescence of Y-based fluorides: from $NaYF_4$: Yb/Er to YF_3: Yb/Er crystals, Nanotechnology. 31 (50) (2020) 505605.
[3] Y. Wang, F. Hong, L. Yu, H. Xu, G. Liu, X. Dong, W. Yu, J. Wang, Construction, energy transfer, tunable multicolor and luminescence enhancement of YF_3: RE^{3+} (RE=Eu, Tb)/carbon dots nanocomposites, J. Lumin. 221 (2020) 117072.
[4] X. Cui, H. Wu, T. Hu, J. Zhang, X. Zhong, X. Wu, J. Wang, X. Li, J. Yang, C. Gao, Pressure effect on the ionic transport behavior and dielectric property of YF_3, J. Alloy. Compd. 823 (2020) 153866.
[5] B.J. Liu, M. Gu, X.L. Liu, Effect of Li^+ and Zn^{2+} Co-doping on luminescent properties of Gd_2O_3:Eu^{3+} nanoparticles, Journal of the chinese rare earth society. 25 (2) (2007) 162–166.
[6] L. He, L. Xia, Y. Yang, Q. Zheng, N. Jiang, C. Xu, Y. Liu, D. Lin, Morphology-controlled synthesis, growth mechanism and fluorescence of YF_3: Eu^{3+}, Bi^{3+}, Mater. Res. Bull. 95 (2017) 483–490.
[7] A.C. Yanes, A. Santana Alonso, J. Méndez Ramos, Novel Sol-Gel Nano-Glass–Ceramics Comprising Ln^{3+}-Doped YF_3 Nanocrystals: Structure and High Efficient UV Up-Conversion, Adv. Funct. Mater. 21 (2011) 3136–3142.
[8] M. Darbandi, T. Nann, One-pot synthesis of YF_3@silica core/shell nanoparticles, Chem. Commun. (7) (2006) 776.
[9] S.S. Nanda, P. Nayak, S. Dash, Structure, morphology and luminescent properties in Eu^{3+} activated (Y, Gd)$_6$3 nanophosphors, Dae Solid State Physics Symposium. 2115 (2018) 030150–030154.
[10] C. Wang, X. Mu, J. Huo, B. Zhang, K. Zhang, Highly-efficient SERS detection for E. coli using a microfluidic chip with integrated $NaYF_4$:Yb, Er@Si_O2@Au under near-infrared laser excitation, Microsyst. Technol. 27 (9) (2021) 3285–3291.
[11] P. Verma, K. Mori, Y. Kuwahara, R. Raja, H. Yamashita, Plasmonic nanocatalysts for visible-nir light induced hydrogen generation from storage materials, Mater. Adv. 2 (3) (2021) 880–906.
[12] Z. Hu, C. Fang, B.o. Li, Z. Zhang, C. Cao, M. Cai, S. Su, X. Sun, X. Shi, C. Li, T. Zhou, Y. Zhang, C. Chi, P. He, X. Xia, Y. Chen, S.S. Gambhir, Z. Cheng, J. Tian, First-in-human liver-tumour surgery guided by multispectral fluorescence imaging in the visible and near-infrared-I/II windows, Nat. Biomed. Eng. 4 (3) (2020) 259–271.
[13] Y. Liu, S. Liu, H. Peng, X. Wang, L. Zhang, L. Zhu, D. Zhang, J. Guo, Structural design and synthesis of new MoO_{3-x} interlayer bi-functional nanomaterials for enhanced up-conversion luminescence properties, Adv. powder tech. 32 (6) (2021) 2053–2063.
[14] M. Wang, Z. Yang, Y.F. Wang, Preparation and characterization of $NaGdF_4$: Eu^{3+}/AAO thin films, Chemical Journal of Chinese Universities. 32 (5) (2011) 1037–1042, in Chinese.
[15] Y.R. Lyu, T.E. Hsieh, The effect of dielectric confinement on photoluminescence of In_2O_3-SiO_2 nanocomposite thin films incorporated by nitrogen, J. Appl. Phys. 113 (18) (2013) 962–972.
[16] M. Massaro, C. Viseras Iborra, G. Cavallaro, C.G. Colletti, F. García-Villén, G. Lazzara, S. Riela, Synthesis and characterization of nanomaterial based on halloysite and hectorite clay minerals covalently bridged, Nanomaterials. 11 (2) (2021) 506.
[17] H. Peng, D. Wu, H. Wan, LuLu Jia, G. Chen, J. Li, Y. Cao, X. Liu, R. Ma, Facile synthesis and characterization of halloysite@$W_{18}O_{49}$ nanocomposite with enhanced photocatalytic properties, Appl. Clay Sci. 183 (2019) 105319.
[18] V. de Abreu Pereira, I. dos Santos Paz, A.L. Gomes, L.A. Leite, P.B.A. Fechine, M. de sá Moreira de S. Filho, Effects of acid activation on the halloysite nanotubes for curcumin incorporation and release, Appl Clay Sci. 200 (2021) 105953.
[19] Y.R. Song, P. Yuan, P.X. Du, A novel halloysite-CeOx nanohybrid for efficient aresenic removal, Appl. Clay Sci. 186 (2020) 105450–105460.
[20] S. Lin, S. Li, Y. Zhang, T. Ma, H. Huang, All-in-one polarized Cd/CdS/halloysite ferroelectric hybrid for exceptional photocatalytic hydrogen evolution, J. Mater. Chem. A. 9 (33) (2021) 17936–17944.
[21] Y. Jian, H. Guo, S.L. Chen, Anchor and space-confinement effects to form ultrafine ru nanoclusters for efficient hydrogen generation, J. Mater. Chem. A. 6 (2018) 13859–13866.
[22] D. Hiller, D. Tröger, M. Grube, D. König, T. Mikolajick, The negative fixed charge of atomic layer deposited aluminium oxide-a two-dimensional SiO_2/AlOx interface effect, Journal of Physics D: Applied Physics 54 (27) (2021) 275304.
[23] T. Takagahara, Effects of dielectric confinement and electron-hole exchange interaction on excitonic states in semiconductor quantum dots, Phys Rev B Condensed Matter. 47 (8) (1993) 4569–4575.
[24] M. Zhao, P. Liu, Halloysite nanotubes/polystyrene (HNTs/PS) nanocomposites via in situ bulk polymerization, J Therm Anal Calorim. 94 (1) (2008) 103–107.
[25] Wen, S., M. A., Shi, J. J., 2011. Surface modification of long-chain alkyl silane on HNTs. *Silicone Material.* 25(4), 248-252.
[26] S. Li, P. Wu, H. Li, N. Zhu, P. Li, J. Wu, X. Wang, Z. Dang, Synthesis and characterization of organo-montmorillonite supported iron nanoparticles, Appl Clay Sci. 50 (3) (2010) 330–336.
[27] K. Lim, W.S. Chow, S.Y. Pung, Enhancement of thermal stability and UV resistance of halloysite nanotubes using zinc oxide functionalization via a solvent-freeapproach, Metall. Mater. Trans. *A. Phys. Metall. Mater. Sci.* 026 (006) (2019) 787–795.
[28] K. Ravichandran, E. Sindhuja, Fabrication of cost effective g-C_3N_4-Ag activated ZnO photocatalyst in thin film form for enhanced visible light responsive dye degradation, Mater. Chem. Phys. 221 (2019) 203–215.
[29] W. Guo, W. Liu, L.i. Xu, P. Feng, Y. Zhang, W. Yang, C. Shuai, Halloysite nanotubes loaded with nano silver for the sustained-release of antibacterial polymer nanocomposite scaffolds, J Mater Sci Technol. 46 (2020) 237–247.
[30] Y. Wu, D. Yang, X. Kang, P. Ma, S. Huang, Y. Zhang, C. Li, J. Lin, Core–shell structured luminescent and mesoporous β-$NaYF_4$:Ce^{3+}/Tb^{3+}@mSiO_2-PEG nanospheres for anti-cancer drug delivery, Dalton Trans. 42 (27) (2013) 9852.
[31] C. Gong, Q. Li, R. Liu, Y. Hou, J. Wang, X. Dong, B.o. Liu, X. Tan, J. Liu, K.e. Yang, B. o. Zou, T. Cui, B. Liu, Structural phase transition and photoluminescence properties of YF_3:Eu^{3+} nanocrystals under high pressure, Phys. Chem. C. 118 (39) (2014) 22739–22745.